Fault detection in a physically redundant MEMS accelerometer array

Daniel Watson[1], and Dr. Karl Reichard[2]

[1,2] *Pennsylvania State University, State College, PA, 16802, United States*
duw428@psu.edu
kmr5@psu.edu

ABSTRACT

The latest generation micro-electro-mechanical system (MEMS) accelerometers offer high bandwidth and low noise floors previously limited to piezoelectric transducer (PZT) based sensors. These relatively low cost MEMS sensors drastically expand the financially practical applications for high frequency, vibration based, prognostic health management (PHM). This paper examines a physically redundant array of MEMS accelerometers for applications where sensor access after deployment is difficult or infeasible. Three identical single axis MEMS accelerometers were placed in an array for testing. Instead of a typical tri-axial configuration, the three sensors were placed with a common sensitivity axis. The construction and basic performance parameters of the MEMS array is discussed. Signal correlation was chosen as a condition indicator (CI) to use in conjunction with majority voting to determine sensor operating status. Signal correlation is reviewed and various synthesized signals were analyzed to study the anticipated cross-correlation of different waveforms. The theoretical effect of sensor noise was analyzed to determine its impact on the method. Auto-correlation was used with previously collected vibration data to confirm feasibility with real world signals. Subsequent measurements with the physically redundant array of impulses and motor vibration show the feasibility of implementing robust MEMS accelerometer arrays using the latest generation of high bandwidth MEMS accelerometers. Planned future work includes deploying the sensor array on tribology test equipment to validate MEMS sensor effectiveness compared to traditional PZT based accelerometers for the detecting of scuffing faults.

1. BACKGROUND

Traditionally, vibration fault monitoring has been performed using integrated electronic piezoelectric (IEPE) based accelerometers which offered superior sensitivity, noise density levels, and bandwidth than other accelerometer configurations. The IEPE accelerometers, also known as ICP accelerometers (ICP is a trademark of PCB Piezotronics), integrate a pre-amplifier circuit into the transducer to isolate the transducer from output impedance loads and reduce transmission noise (Instruments, 2019; Pizotronics, n.d.).

IEPE accelerometers are an excellent choice for many systems but have inherent shortcomings that restrict their operating environment. IEPE sensors often require instrument grade DC power supplies operating between 18 and 30 volts and currents up to 2 mA (Pizotronics, n.d.). The relatively high supply voltage and current requirements limits their application in remote, battery powered, situations. The high cost of system components also limits their use to research and development activities and high capital cost systems such as aerospace PHM. Power supply and system cost prohibitions for IEPE accelerometers leave a substantial niche in PHM - small, low power draw, inexpensive accelerometers. Micro electro mechanical system (MEMS) accelerometers are a rapidly maturing technology, relegated until recently to low bandwidth applications, poised to take over even high performance requirement applications (Piezotronics, n.d.).

MEMS accelerometers are fabricated using microelectronic fabrication techniques, typically using a silicon semiconductor base, similar to computer chip manufacturing. The ability to produce sensor elements using semiconductor manufacturing techniques leads to very compact, low cost sensors. Commercially available MEMS accelerometers are typically integrated with a pre-amplifier similar to IEPE accelerometers providing an analog signal output (Piezotronics, n.d.). Figure 1 shows the ADXL10005z, a single axis MEMS accelerometer installed with an analog anti-aliasing filter on a printed circuit board measuring just 20 mm (0.8 inches) on a side. Table 1 compares the bandwidth and noise density of the ADXL1005 MEMS accelerometer to the lower bandwidth model family member ADXL1001, the previous generation ADXL001 MEMS accelerometer, and two high performance piezoelectronic accelerometers; the low noise PCB 352C04

Table 1. Sensor array sensitivity.

Sensor	Spectral noise at $100Hz$	Resonant frequency
ADXL1005	75 $[\frac{\mu g}{\sqrt{Hz}}]$	$42\,kHz$
ADXL1001	30 $[\frac{\mu g}{\sqrt{Hz}}]$	$21\,kHz$
ADXL001	4000 $[\frac{\mu g}{\sqrt{Hz}}]$	$22\,kHz$
PCB 352C04	8 $[\frac{\mu g}{\sqrt{Hz}}]$	$> 50\,kHz$
PCB 352A60	40 $[\frac{\mu g}{\sqrt{Hz}}]$	$> 95\,kHz$

and the high bandwidth PCB 352A60. A trend shown by the ADXL100x and PCB 352xxx series is a trade-off of higher bandwidth at the expense of additional spectral noise.

The reliability of PHM system components is essential for their successful application. The system must be capable of operating in their employed environment, and ideally systems would be able determine their operating status. Applications such as satellites in space, autonomous vehicles, and remotely operated manufacturing facilities are all possible applications of reliable and robust sensor systems. Some MEMS accelerometers have on-board self-test capabilities (*ADXL1005Z Evaluation Board*, n.d.). Beyond determining operating status it would be ideal if there are system redundancies to permit continued PHM after an instrument fault detection (IFD) event. Paul Frank explores the merits of analytical (functional) and physical redundancy to isolate IFD and component fault detection (CFD) events (Frank, 1990). Analytical redundancy uses system relationships to provide redundant information, e.g. using the temperature measurement from a thermal-couple at location A to estimate air pressure at location B to provide redundancy to a pressure gauge.

Physical redundancy uses multiple sensors measuring the same variable. Physical redundancy using majority voting logic does not require a priori knowledge of system relationships and is typically more computationally efficient to implement, these characteristics make physical redundancy appealing when developing a system that can be widely deployed on a variety of platforms. Frank argued that the high cost of physical redundancy was a limiting factor and was a proponent of analytical redundancy - requiring significant system level knowledge to implement (Frank, 1990). The low cost of MEMS accelerometers make it feasible to utilize multiple, redundant, sensors with self-testing and cross-correlation algorithms providing insight into PHM system status.

2. MEMS SENSOR ARRAY

The prototype MEMS sensor array of this work is based on the Analog Devices AD1005z evaluation board. The evaluation board consists of the Analog Devices AD1005 high bandwidth MEMS accelerometer mounted on a printed circuit board with a power supply decoupling capacitor and a resistor-capacitor low pass anti-aliasing filter with a -3dB bandwidth of 20 kHz. The evaluation board was chosen for its availability and convenience, planned future versions will use a custom circuit board to reduce the physical footprint of a three sensor array. The prototype array is mounted on a machined aluminum mounting block that locates the sensitivity axis of the sensors co-linear with the the mounting bolt. A shear mode ICP accelerometer, a PCB 352A60, is also mounted for initial troubleshooting. The assembled MEMS accelerometer array, minus wiring, is shown in Figure 1.

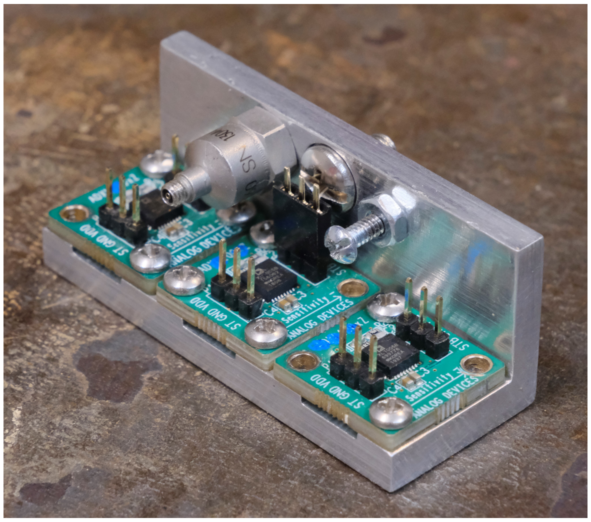

Figure 1. MEMS accelerometer array prototype.

A GW Instek GPC-30300 lab grade DC power supply is used to provide 5 VDC to the MEMS sensors while a National Instruments PXI-1031 chassis with a PXI-4472B card was used for data acquisition (DAQ) including the ICP accelerometer. The sampling rate, unless otherwise specified, was 102400 Hz - the maximum sampling rate of the PXI-4472B card. A control panel with switches to individually activate the Self Test and Standby features of the MEMS accelerometers was used as an interface between the DAQ and the array.

2.1. Calibration

System calibration was performed using a PCB 394C06 handheld calibrator operates at $159\,Hz$ and was set to an excitation amplitude of $1\,g\,RMS$. The ADXL1005 MEMS accelerometer has a ratiometric sensitivity meaning the output sensitivity is proportional to power supply voltage [VDD], the fixed $5\,VDC$ output of the power supply was used for testing in this work.

As seen in Table 2 there is noticeable sensor to sensor differences in sensitivity, values provided in Table 2 were obtained with a supply voltage of $5.0364\,VDC$. Calibration

Table 2. Sensor array sensitivity.

Sensor	**Sensitivity** $[\frac{g}{Volt}]$
ADXL1005z A	45.1764
ADXL1005z B	45.2323
ADXL1005z C	49.9702
PCB 352A60	93.2522

Table 3. Power supply isolation.

Calibrator status and sensor	**Acceleration** $[g\,RMS]$
OFF, Sensor A	0.0447
OFF, Sensor C	0.0250
ON, Sensor A	0.9746
ON, Sensor C	0.0246

was performed at the start of each test sequence and periodically throughout data collection. Calibration was performed in the frequency domain using a three second long sample. Time domain data was windowed using an amplitude adjusted Hann window. The power spectral density in units of $\frac{Volts^2}{Hz}$ is calculated, the peak energy frequency bin is identified (at $159\,Hz$) and its energy is used to calculate the sensor sensitivity using the known calibration amplitude of $1\,g\,RMS$.

2.2. Sensor noise floor

All measurements have some degree of uncertainty to them both systematic and random. Proper calibration of a sensor helps minimize systematic error. Even after calibration a measurement chain consisting of sensing element, internal pre-amplifier, cabling, and data acquisition system has a noise floor characteristic to the measurement chain. To measure the noise floor, the MEMS array was mechanically isolated from vibration using thick open cell foam placed on a cast iron assembly table. A one second long data sample was collected of the isolated MEMS array and the signal analyzed. As the MEMS array was static the measured signal represents system noise.

Accelerometer noise is typically provided by the manufacturer in units of $\frac{\mu g}{\sqrt{Hz}}\,RMS$ and is therefor dependent on system bandwidth. The evaluation boards have a built in low pass anti-aliasing filter at $20\,kHz$, but the the measurement is made at a sampling rate of $102400\,Hz$, so the effective bandwidth is the Nyquist frequency of $51200\,Hz$. Analog Devices specifies a noise density of $75\,\frac{\mu g}{\sqrt{Hz}}$. Using Eq. (1) (Devices, n.d.) the expected noise from just the sensor is $0.0215\,g\,RMS$.

$$Noise = Noise\,Density * \sqrt{bandwidth * 1.6} \qquad (1)$$

The RMS noise floor of the measurement chain for the full bandwidth of $51200\,Hz$ was measured for Sensor C of the MEMS array at $0.0250\,g\,RMS$. The measured noise floor is close to the expected noise from just the sensor and indicates that the measurement chain is minimally contributing to system noise. These results also emphasize the importance of using low noise density accelerometers as the MEMS accelerometer is likely the major source of noise in the measurement.

2.3. Power Supply Isolation

For true physical redundancy, the three MEMS sensors in an array should have independent power supplies and grounds. Design constraints including space and cost may necessitate a common power supply. The system reliability of a common power supply verse independent power for each sensor should be considered during the design of a redundant array. In the prototype MEMS array used in this work, a common power supply was desired for simplicity. Sensor independence was tested by mechanically isolating Sensor C while Sensor A was excited with the PCB394C06 calibrator. Ideally the physically isolated and static sensor, Sensor C, would produce the same readings independent of Sensor A excitation. Table 3 provides RMS acceleration values for Sensors A and C for successive test runs, the initial run is with Sensor A mounted to the inactive calibrator. The second run, performed immediately after, has the calibrator active with a nominal acceleration of $1\,g\,RMS$. The results shown by Table 3 indicate sensor output of the ADXL1005z evaluation boards is independent with a common power supply. Sensor C measurements in both cases matched the sensor noise floor measurements conducted earlier. The elevated measurement for Sensor A with the calibrator off can be attributed to the calibrator placement on a non-isolated workbench instead of open cell foam. The measurement independence with a common power supply allows initial testing with a simplified design; however, for true physical redundancy, independent power supplies should be used for each channel.

3. SENSOR FAULT DETECTION

As discussed earlier, sensor redundancy can be accomplished in variety of ways ranging from simplistic physical redundancy to sophisticated functional redundancy that requires extensive system level knowledge to implement. Physical redundancy incurs increased equipment costs (Stork & Kowalski, 1999). Recent advancements in MEMS accelerometers allow for high performance applications using relatively cheap sensors - facilitating the use of simple physical redundancy and rapid implementation on new applications. To capitalize on low cost sensors, a majority voting scheme is proposed for a physically redundant MEMS accelerometer array.

For the $N = 3$ sensor array used in this work there are multiple methods to implement majority voting. A common implementation of majority voting is using each sensor measurement to calculate a condition indicator (CI) and when a majority of sensors (2 or more for an $N = 3$ array) agree, the result with majority is accepted as the valid result. For the prototype array in this work it was desired to know the sensor operating condition of the array independent of system fault CI's. Signal correlation, a measure of similarity of two signals, provides an excellent sensor operational check when combined with majority voting in a physically redundant array.

3.1. Signal correlation

Correlation is a time domain based concept that is a measure of how similar two signals are. The terms auto- and cross-correlation are used when comparing a signal to itself or to a separate signal respectively. Conceptually correlation is calculated by multiplying two time domain signals together element-wise, integrating with respect to time the element-wise products, and normalizing for signal duration. This multiplication and integration is performed for all possible relative time differences between the two signals, after each correlation calculation the element-wise multiplication pairs are shifted by one time step. The net time shift, or delay, is denoted as Tau. Cross-correlation in the time domain can be notated using conjugation as shown by equation (2)

$$R_{xy}(\tau) = \frac{1}{T} x(-t) \otimes y(t) \tag{2}$$

where $\otimes$ is the operative representing conjugation.

The result of this process for auto-correlation is a vector of values with maximum value when there is no relative shift between the signals. When there is no shift, all element-wise multiplications will have matching signs, always resulting in a positive valued product, maximizing the element-wise product integral . As relative shift between the two signals occurs there will be element-wise operations where negative and positive values are multiplied - reducing the magnitude of the integral (Gabrielson, 2018).

3.2. Correlation calculation

While straightforward in explanation, correlation is computationally expensive to calculate in the time domain. Fortunately, efficient computation of correlation is possible in the frequency domain thanks to the Fast Fourier Transform. A brief description of the frequency domain calculation of correlation follows. If we let x and y represent our time domain data, X and Y represent their respective discrete Fourier transforms - their linear spectra, and

$$X = F[x] \tag{3}$$

and

$$x = F^{-1}[X] \tag{4}$$

where F and F^{-1} are the discreet Fourier and inverse Fourier transform operatives. Also note the inverse discrete Fourier transform of a complex conjugate produces the time reversed complex conjugate in the time domain as shown in equation (5),

$$x^*(-t) = F^{-1}[X^*]. \tag{5}$$

When calculating correlation we are dealing with data that originated in the time domain and are thus all real, the complex conjugate does not change a real value. We can thus write $x^*(-t)$ without denoting the complex conjugate as the equivalent $x(-t)$.

It is also important to note that the inverse Fourier transform of two frequency domain linear spectra is equivalent to the convolution of their time domain vectors. Following from equation (5) and written as cross-correlation we have the result,

$$F^{-1}[X^* Y] = x^*(-t) \otimes y(t), \tag{6}$$

which is a simple time normalization away from the correlation definition of equation (2) (Gabrielson, 2018).

3.3. Correlation theoretical performance

As noted above, auto and cross-correlation differ simply by the use of the same or different signal vectors for the second term in the product pair. In a physically redundant pair the difference between the two types of correlation is blurred as the the signals from any sensor pair are nominally identical. Due to this, the expected cross-correlation performance closely matches the theoretical results of a signals auto-correlation. For simplicity the performance of auto-correlation of common signal phenotypes will be explored, followed by auto-correlation of real world signals, an analyses on the impact of sensor noise on auto-correlation, and expected results of common sensor faults for cross-correlation.

3.3.1. Auto-correlation of typical artificial signals

An understanding of expected results from a variety of signals is essential to contextualize the application of correlation to a physically redundant MEMS accelerometer array. Four classes of signals are explored; low and high frequency sinusoids (relative to signal length), multi-tone sinusoidal signals, random noise signals, and impulsive signals.

Low frequency sinusoids, for the purpose of correlation calculations, are defined as those with periods longer in length than the time signal analyzed. This important distinction is due to the repetition of waveform features that occurs with waveforms of relatively higher frequency. Long waveform periods relative to signal length prevent the time-alignment of signals at time shifts of one period for uniform waveforms. This is most clearly shown in Figures 2 and 3 showing auto-correlation of a one second signal with sinusoids of amplitude of $1\,g$ and frequencies of $1\,Hz$ and $10\,Hz$. The high frequency signal in Figure 3 has multiple correlation peaks with spacing of one time period of the signal sinusoid.

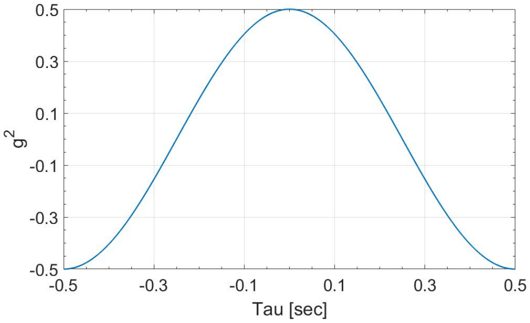

Figure 2. Low frequency sinusoid auto-correlation.

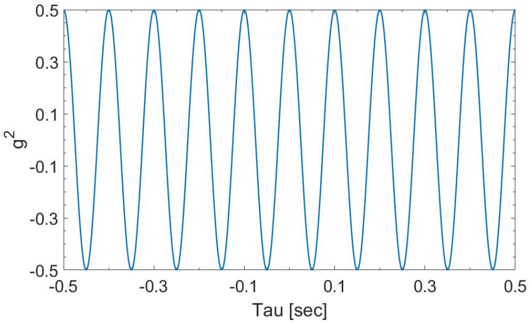

Figure 3. High frequency sinusoid auto-correlation.

For the purpose of sensor fault detection in a physically redundant array, a single sharp peak in cross sensor correlation is desired. A single sharp peak with minimal noise floor will allow algorithms to readily detect nominal performance with a high degree of probability. Figures 2 and 3 show a catch-22 when using pure sinudoidal signals for correlation calculations, any tonal signal of low enough frequency to prevent repetitive peaks in correlation will have a broad peak in correlation. The broad response curve of sinusoidal auto-correlation is due to adjacent signal samples dependence on nearby values (e.g. sample 8 is highly correlated to sample 9). This is clearly seen in Figure 4 where a $1\,Hz$ signal is shifted by a delay of $\frac{\pi}{6}\,radians$ and plotted with the original signal. As seen in Figure 4, for any given sample time the sign of the two signals is likely to agree, increasing the element-wise integral inherent in correlation calculation and producing the characteristic broad peak of sinusoid auto-correlation.

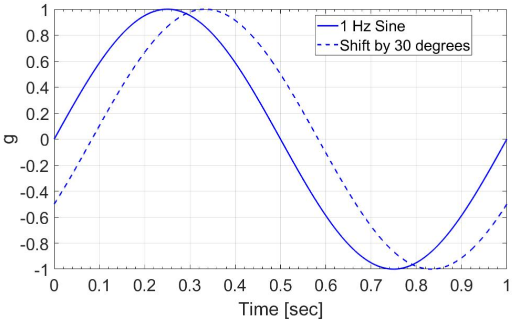

Figure 4. Sinusoid with phase delay overlay.

Single tone sinusoids do not produce sharp correlation peaks as desired for our sensor operation check, but real world signals are often comprised of multiple tones. Especially when the tonal components are non-integer multiples, a multi-tonal signal allows for the relaxation of our high frequency limit. Figure 5 is the auto-correlation of a one second long signal comprised of equal magnitude tones at $17\,Hz$, $23\,Hz$, and $31\,Hz$, the three frequencies chosen are the 7^{th}, 9^{th}, and 11^{th} prime numbers and have a lowest common multiple of $12121\,Hz$. Figure 5 exhibits the expected auto-correlation peak at zero time shift, however the rapidly and widely fluctuation correlation signal is inappropriate to use for the sensor cross-correlation operation check.

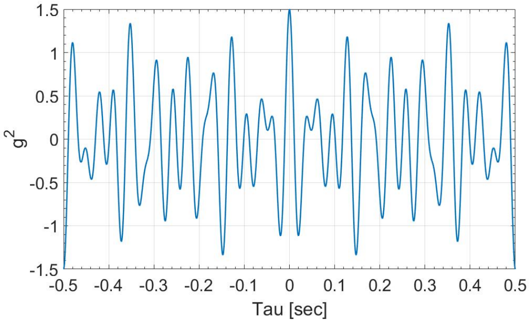

Figure 5. Multi-tonal signal auto-correlation.

As shown above, signal- and multi-tone sinusoidal signals are not valid waveforms to perform sensor cross-correlation checks. Lessons learned from the prior examples include using a waveform without periodically repeating segments and a waveform where neighboring samples are independent of each other. Two signal types commonly used in signal analysis immediately spring to mind that comply with our lessons learned; the random noise and impulse signals.

To generate a random noise signal the MATLAB function *randn* was used, providing a one second long sample of normally distributed pseudo-random numbers at a sampling rate of $102400\,Hz$. The impulse signal follows the convention of containing a single non-zero value that integrates to a non-dimensional 1.0 using equations (7) and (8) where Δt is the inverse of sampling rate (Gabrielson, 2018)

$$\sum_{n=1}^{N} \delta_n \Delta t = 1 \tag{7}$$

$$\delta_n = [\frac{1}{dt}, 0, 0, 0, ...]. \tag{8}$$

Figures 6 and 7 show auto-correlation results from random noise and impulsive signals, respectively. Immediately evident is the similarity between auto-correlations of the two signals which are vastly different. The impulse signal's auto-correlation is a singular peak at zero time shift and zero for all other time shifts. This is the expected result for a signal that has non-zero amplitude for only one time value. The, possibly, surprising result is the auto-correlation of a random noise signal as shown by Figure 6. Contrary to the broad peaks of the sinusoid signals, the random noise signal produces an auto-correlation very similar to the impulsive signal. At zero time shift all values have matching sign and thus increase the integral in the correlation calculation. At all other time shifts the random nature of the signals produces auto-correlation values near zero.

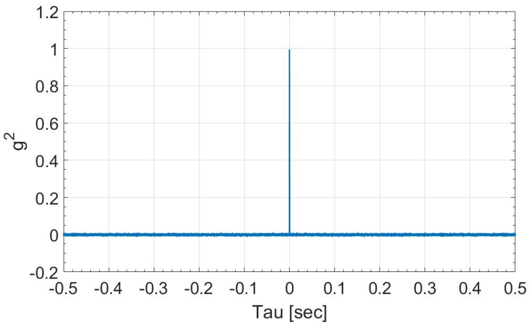

Figure 6. Random noise auto-correlation.

The auto-correlation results of Figures 6 and 7 are very promising for the use of random and impulsive signals. A singular peak at zero time shift and a relatively low noise floor at all other values for auto-correlation should produce nearly identical results for cross-correlation between physically redundant MEMS accelerometers. While the above results are promising, real world signals are unlikely to be purely random or perfectly impulsive and are studied next.

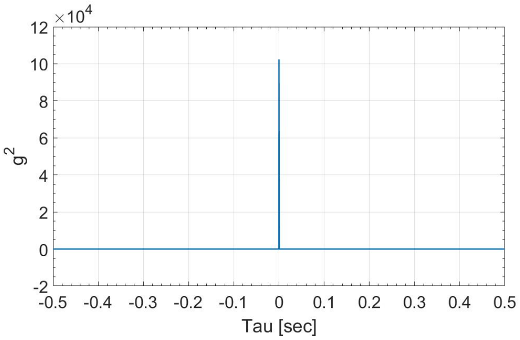

Figure 7. Impulse signal auto-correlation.

3.3.2. Auto-correlation of real world signals

Signals representative of real world data were used to investigate the applicability of correlation for sensor function checks of in-situ physically redundant MEMS accelerometer arrays. As an initial check, auto-correlation was calculated to see if the signals were conducive to sensor function checks. Once the auto-correlation was analyzed the effects of sensor noise was investigated to more closely align with the realities of a sensor array. Two different classes of signals were used. An impulsive signal from a wind turbine with pinion gear fault, and a second order cyclostationary signal from a healthy roller element bearing.

The first dataset analyzed was from a 3 megawatt wind turbine, the vibration readings for the data labeled 'Case 1' were considered high, and the turbine was pulled off-line for inspection. A faulty pinion gear was diagnosed ('Bechhoefer, n.d.). The impulsive waveform typically seen in gear faults was viewed as a good test case for correlation based sensor function tests based on the results of the perfectly impulsive test signal used in Figure 7. This dataset was recorded with a sampling rate of $97656\,Hz$ and the units of acceleration were not noted so the arbitrary unit of Waveform Units $[WU]$ is used in Figure 8 below. The resulting auto-correlation show a distinct singular peak in correlation with high signal-to-noise ratio (SNR) that can clearly be differentiated from an uncorrelated signal such as Figure 10.

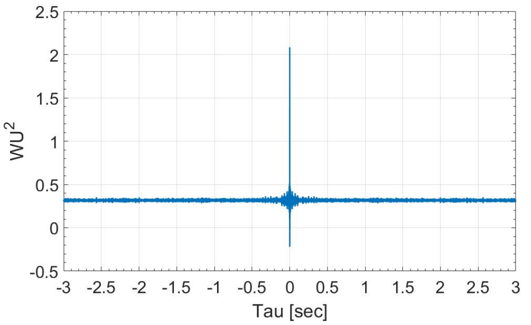

Figure 8. Windmill pinion gear fault auto-correlation.

The impulsive gear fault from the wind turbine data was viewed as the easier signal type for correlation based sensor fault detection. To provide a more challenging use case, vibration data from a healthy roller element bearing was also analyzed. Roller element bearings are considered second order cyclostationary - they have fundamental fault frequencies which have random variation about a mean value due to the imperfect motion of roller elements inside the bearing races (Roque et al., 2009). The fundamental fault frequencies for an inner race, outer race, roller element, or cage fault would be expected to dominate the signal for a fault of a given type. The date sample used was from the start of a bearing fault test on a nominally healthy bearing (Lee, Qiu, Yu, Lin, & Services, 2007), the resulting data is not dominated by any faults and is typical for bearing data collected in-situ on industrial equipment. Figure 9 shows the resulting auto-correlation and indicates that typical roller element bearing vibration data is conducive to correlation based sensor fault detection albeit with a greater noise floor.

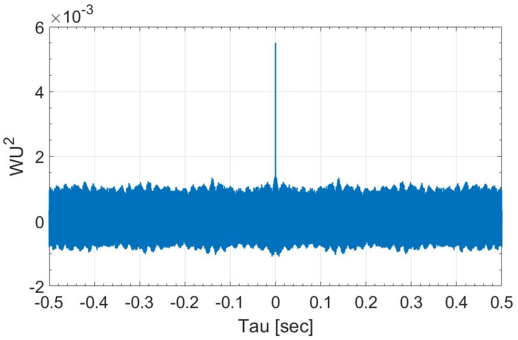

Figure 9. Healthy bearing vibration auto-correlation.

3.3.3. Correlation resilience to sensor noise

Thus far we have only looked at the auto-correlation of synthetic and legacy real world signals. In a physically redundant MEMS accelerometer array the individual sensors are independently subject to sensor noise. According to the manufacturer of the MEMS accelerometers used in this work, the sensor noise has a Gaussian distribution and is uncorrelated to external influence (Devices, n.d.). Figure 10 shows the theoretical cross-correlation between two truly independent sensors with the same noise density specifications as the ADXL1005 sensor. Figure 11 shows the empirical cross-correlation between Sensors A and C when Sensor C is physically isolated from Sensor A and the sensors are nominally static.

The theoretical results show the random noise expected from the cross-correlation of uncorrelated signals. The empirical results using two of the sensors from the MEMS accelerometer array show that the signals are not completely uncorrelated; however, an inspection of the y axis shows minimal range in correlation values and no clear separation between the gradual peak and the noise floor. Also of note is the non-zero dc offset of the cross-correlation which is unique to this particular dataset. Overall, the results of sensor noise independence are satisfactory for the application.

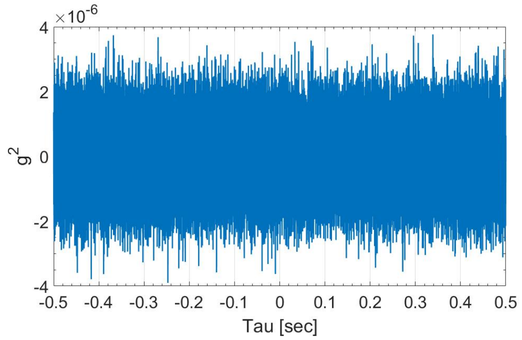

Figure 10. Theoretical sensor noise cross-correlation.

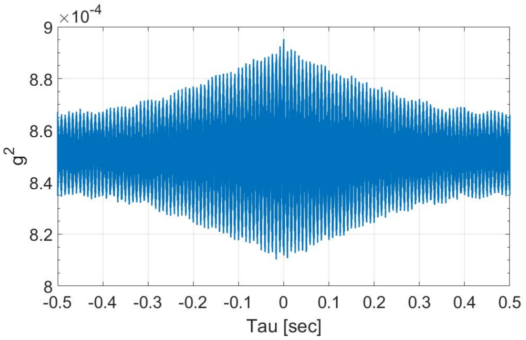

Figure 11. Empirical sensor noise cross-correlation.

The effect of independent sensor noise was studied for the random noise, impulse signal, and wind turbine gear fault signals used for Figures 6, 7, and 8. Two separate random noise signals were generated *Noise Signal A* and *Noise Signal B*, each random noise signal had a noise density equal to the specification sheet value of the ADXL1005, 75 $\frac{\mu g}{\sqrt{Hz}}$. Instead of performing auto-correlation on the three signals of interest, cross-correlation was used with the first signal containing the base signal with *Noise Signal A* superimposed, and the second component of cross-correlation using the same base signal but *Noise Signal B* superimposed. This simulates two sensors on a physically redundant MEMS accelerometer array measuring the same vibration signal. If the sensor noise is low enough, there will be minimal impact between a signals auto-correlation and the simulated cross-correlation.

After the addition of independent sensor noise the theoretical cross-correlation was calculated for the random noise, impulse signal, and wind turbine gear fault signals of Figures 6, 7, and 8. Figures 12, 13, and 14 show the resulting cross-correlation which are functionally identical to their corresponding auto-correlation results. This indicates that correlation based sensor fault detection is resilient to sensor noise from the MEMS accelerometers used.

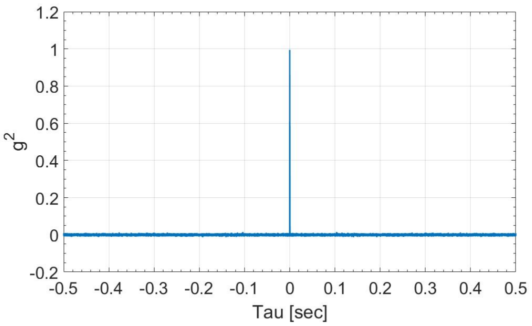

Figure 12. Random noise with sensor noise cross-correlation.

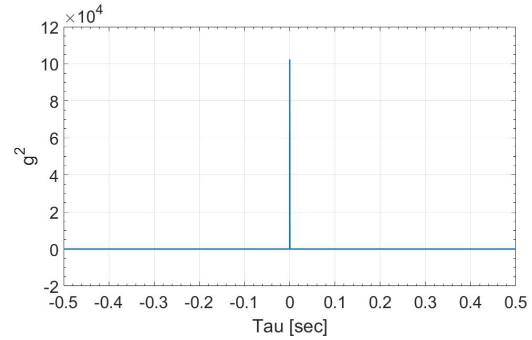

Figure 13. Impulse signal with sensor noise cross-correlation.

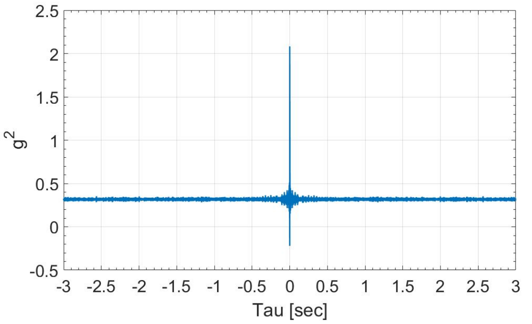

Figure 14. Windmill pinion gear fault with sensor noise cross-correlation.

3.3.4. Theoretical cross-correlation with healthy sensors

Starting with our well understood random noise signal cross-correlation, Figure 15 shows the cross-correlation results anticipated for a healthy array. Each of the three sensors - Sensor A, Sensor B, and Sensor C are experiencing the same base signal with their respective independent sensor noise superimposed. As shown above, sensor noise has minimal effect so the expected results for the three cross-correlations is that of a random noise signal auto-correlation. As seen in Figure 15 the three possible cross-correlation pairs match with sharp peaks and minimal noise floor, this is an idealized result of an array with functioning sensors.

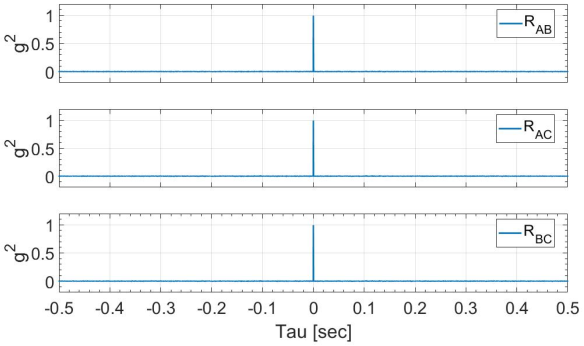

Figure 15. Random noise, healthy array cross-correlation.

3.3.5. Theoretical cross-correlation with sensor faults

The chief advantage of a physically redundant MEMS accelerometer array is the ability to detect when a single sensor is faulty, reject the contribution from the faulty sensor, and continue to provide quality data to the end user. The ability to distinguish between healthy and faulty sensor cross-correlations is critical. Figure 16 showcases the cross-correlation phenotype expected when a single sensor fault results in a vector of zeros for that sensor's data. In the case of Figure 16 the theoretical random noise base signal and sensor noise for Sensor C is set to zero while Sensors A and B remain functional. Because Sensors A and B are functioning correctly their cross-correlation, R_{AB}, will produce a sharp, singular, peak with minimal noise floor. The two cross-correlations with a Sensor C signal component, R_{AC}, and R_{BC}, fail to provide the expected result. In fact the cross correlation for the two fault containing cross-correlations is a uniform zero vector. When a single sensor is faulty, two of the three cross-correlation pairs will show poor correlation results.

If Sensor C failed such that the signal was random noise independent from the signals of Sensors A and B, the idealized cross-correlation result would be that shown in Figure 17. Figures 16 and 17 are functionally identical but can be differentiated by zooming the y-axis. When the individual non-zero time shift cross-correlation values are viewed the difference becomes clear. The noise floor for the later figure is non-zero and randomly distributed instead of identically zero.

The relative performance of R_{AB}, R_{AC}, and R_{BC}, shown in Figures 16 and 17, is the basis for the sensor function majority voting scheme. A touch of confusion arises as the faulty sensor signal component is present in two of the cross-correlation calculations, due to this there are two faulty phe-

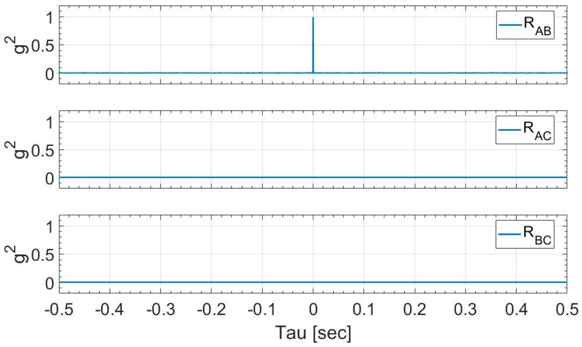

Figure 16. Sensor C reading zero, array cross-correlation.

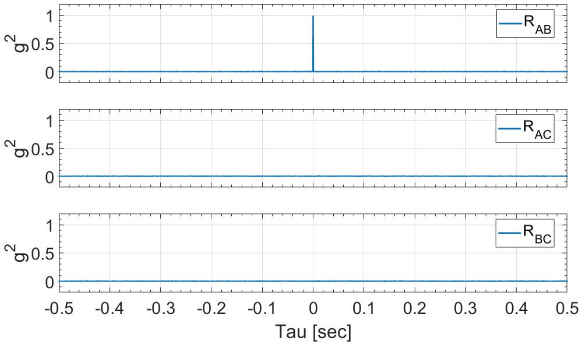

Figure 17. Sensor C uncorrelated, array cross-correlation.

notype cross-correlations in the above plots when only one sensor is providing faulty data. Nonetheless, Sensors A and B are in agreement - evident by the cross-correlation plot of R_{AB}.

The expected makeup of a faulty physically redundant array is a single faulty sensor and two healthy sensors. The opposite is feasible where there are two independent faults and one healthy sensor. When there is only a single healthy sensor the current method is insufficient to identify which sensor, if any, is healthy. Figure 18 displays the idealized result of three sensors with mutually uncorrelated signals as might occur if two (or all three) of the array sensors are providing faulty data. Techniques to identify a single healthy sensor in a physically redundant array are being investigated to supplement the computationally efficient cross-correlation technique.

Based on the theoretical results in Figure 17 it is possible to determine when a single sensor has failed. In the single faulty sensor case the cross-correlation of one pair of sensors provides a nominal result while the other two cross-correlation vectors showcase faulty phenotypes. Continuous, or at least routine, monitoring of the cross-correlation results are necessary to identify instances of a second sensor failure at a later point in time. It is also possible to identify when 2 or more sensors have independent faults as evidenced by complete lack of correlation for R_{AB}, R_{AC}, orR_{BC}. There is the unfortunate possibility of false-positive results when two correlated sensor faults occur. Due to the basic product rule of reliability, the likelihood of two faulty sensors and one healthy sensor returning a false-positive is less than the likelihood of the converse, or the likelihood of a single sensor system failing in isolation.

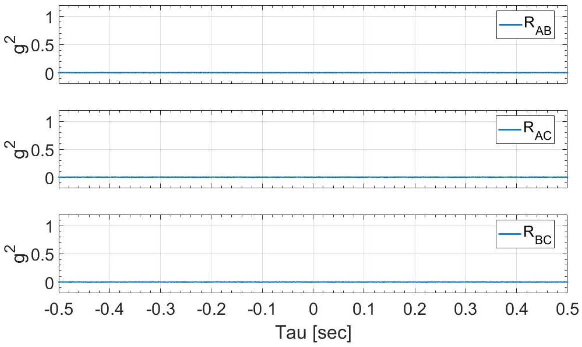

Figure 18. All sensors uncorrelated, array cross-correlation.

3.4. Validation using cross-correlation of MEMS accelerometer array

To empirically validate the theoretical framework discussed above, the physically redundant MEMS accelerometer array was used to collect data in both healthy and faulty configurations. Two types of data were gathered for both healthy and faulty arrays. Impulsive data was collected by placing the MEMS array mount on open cell foam in the orientation shown in Figure 1. Open cell foam was used to isolate the sensor array from external vibrations and simulate free-free boundary conditions, the array was struck normal to the sensitivity axis. Separately, low bandwidth roller element bearing data, $< 10\,kHz$ valid bandwidth, was collected using a magnetic sensor mount placed on the case of a three phase induction motor with the sensitivity axis aligned radially with the roller element bearing. The impulse and motor vibration data provide real world signals similar to the synthesized signals studied previously.

3.5. Healthy MEMS accelerometer array

Prior to data collection the MEMS accelerometer array was physically inspected and then operationally checked by performing a sensor calibration. The array was placed on an isolated section of open cell foam and was struck normal to the sensitivity axis. Figure 19 shows the resulting time domain signals. A three second data sample was used to facilitate manually triggering the DAQ record function and then impacting the array. Figure 20 is the resulting cross-correlation showing the high degree of correlation expected from functioning sensors with an impulsive signal. The three cross-correlation pairs for this impact data have a sharp peak of similar magnitude and a low noise floor.

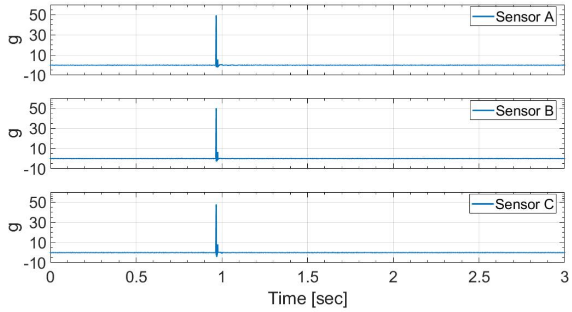

Figure 19. Impact data, healthy array time series.

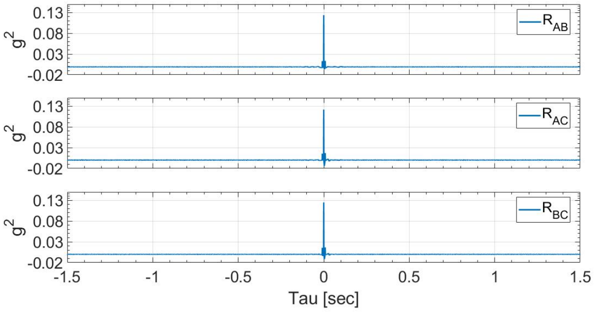

Figure 20. Impact data, healthy array cross-correlation.

Three second samples of induction motor vibration were collected with the MEMS accelerometer array. The motor was running at a nominal $1725\,RPM$ at steady state conditions. The motor used for this dataset had been pulled offline due to audible noise indicating an unknown fault. Figure 21 shows the resulting cross-correlation results. As expected from the theoretical cross-correlation of the bearing dataset shown in Figure 9 there is a higher noise floor than the healthy impact data. In fact this sample had so much tonal background noise the resulting cross-correlations were somewhat inconclusive. After analyzing the initial data, a second set of data was obtained from an identical motor that did not produce audible, tonal, noise. Figure 22 shows the cross-correlation pairs for a healthy array monitoring a nominally healthy motor. A lesson learned is that significant tonal background noise can reduce the effectiveness of cross-correlation sensor fault detection.

3.6. Faulty MEMS accelerometer array

To simulate one possible sensor fault type the four mounting screws used to secure Sensor C were loosened until only two threads of the 4-40 Unified National Coarse (UNC) thread machine screws were engaged in the MEMS array mount. This could simulate either loosened mounting screws due to machine vibration, a mount failure due to vibration fatigue failures, or an installation error.

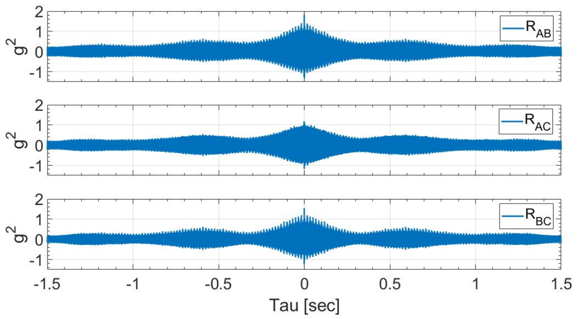

Figure 21. Noisy motor data, healthy array cross-correlation.

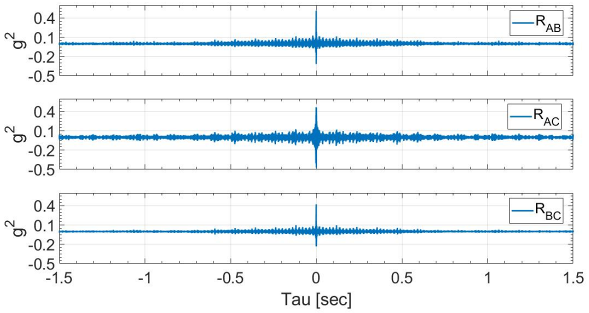

Figure 22. Quiet motor data, healthy array cross-correlation.

Figures 23 and 24 show the result of a loosely mounted Sensor C exposed to an impulsive signal in the time domain and the cross-correlation pairs produced. As seen in the time domain of Figure 23, Sensor C, the ‘faulty’ sensor, has a drastically different impulse response than Sensors A and B. The large negative acceleration peak recorded by Sensor C is evident in the correlation results as the element wise multiplication and integration of correlation produces negative values of correlation and multiple peaks of significant amplitude instead of a singular peak. The noise floor is low due to the physical isolation provided by the open cell foam.

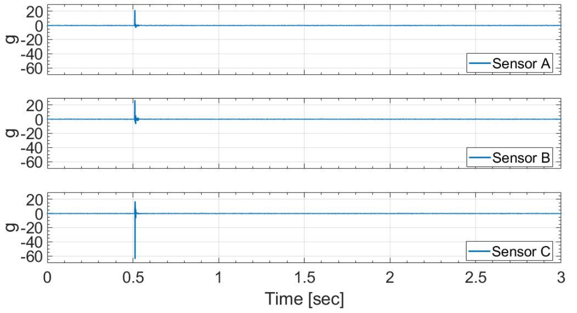

Figure 23. Impact data, faulty array time series.

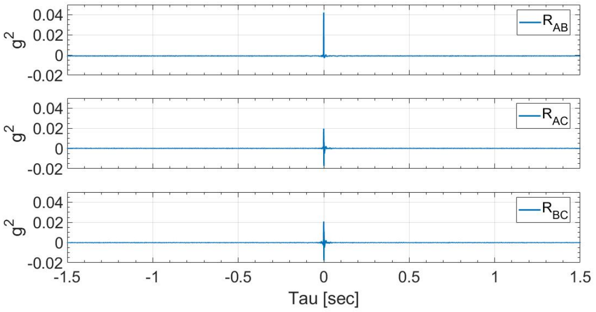

Figure 24. Impact data, faulty array cross-correlation.

Figure 25 revisits the noisy motor of Figure 21 and shows the result when Sensor C is loosely mounted. The relative amplitude differences for R_{AB} between the two figures is a result of motor vibration differences between runs. Despite the generally unfavorable healthy array cross-correlation for the noisy motor measurements, Figure 25 clearly shows a discernible difference when Sensor C is faulty. R_{AB} shows a clear peak and much greater amplitude than the faulted cross-correlation pairs of R_{AC} and R_{BC}. The ability to distinguish the healthy array of Figure 21 and the faulty array of Figure 25 is encouraging.

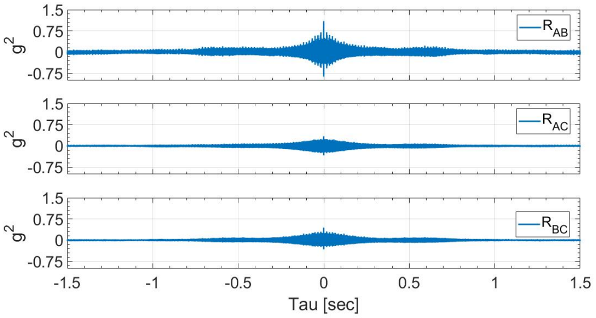

Figure 25. Noisy motor data, faulty array cross-correlation.

4. CONCLUSIONS

Single sensor fault can be detected using majority voting and computationally efficient cross-correlation calculations. Testing shows that the ADXL1005z evaluation boards are suitable for use with a common power supply with minimal impact to sensor output independence. Theoretical results for synthesized signals show that waveforms dominated by random noise or impulsive events produce sharp correlation peaks that are conducive to sensor fault detection. Analysis of real world datasets confirm the applicability of correlation for sensor fault detection.

The physically redundant MEMS accelerometer array was used to collect impulse data and motor vibration data in healthy and faulted conditions. Results from array testing confirm that cross-correlation can be used to identify a single faulty sensor in an array of three physically redundant sensors. Caution is urged when implementing cross-correlation when the signal is dominated by tonal components as first shown by sinusoid auto-correlation and later by real world data of a motor with significant audible tones (Figures 5 and 21). Planned future work includes detection of individual sensor sensitivity drift and installing the physically redundant MEMS accelerometer array on tribology test equipment to detect the initiation of scuffing wear.

REFERENCES

Adxl1005z evaluation board. (n.d.). Retrieved from `https://www.analog.com/en/products/adxl1005.html#product-overview`

'Bechhoefer, E. (n.d.). *High speed gear dataset.* Retrieved from `http://data-acoustics.com/measurements/gear-faults/gear-1/`

Devices, A. (n.d.). *Accelerometer specifications - quick definitions.* Retrieved from `https://www.analog.com/en/products/landing-pages/001/accelerometer-specifications-definitions.html`

Frank, P. M. (1990). Fault diagnosis in dynamic systems using analytical and knowledge-based redundancy. a survey and some new results. *Automatica*, *26*, 459-474. doi: 10.1016/0005-1098(90)90018-D

Gabrielson, T. B. (2018). *Signal analysis.* Unpublished draft manuscript.

Instruments, N. (2019, 3). *Iepe and integrated circuit piezoelectric (icp) explained.* Retrieved from `https://www.ni.com/en-us/innovations/white-papers/18/iepe-and-integrated-circuit-piezoelectric--icp---explained.html`

Lee, J., Qiu, H., Yu, G., Lin, J., & Services, R. T. (2007). Bearing data set ims, university of cincinnati. *NASA Ames Prognostics Data Repository (http://ti.arc.nasa.gov/project/prognostic-data-repository).*

Piezotronics, P. (n.d.). *Introduction to mems accelerometers.* Retrieved from `https://www.pcb.com/resources/technical-information/mems-accelerometers`

Pizotronics, P. (n.d.). *Introduction to icp accelerometers.* Retrieved from `https://www.pcb.com/resources/technical-information/introduction-to-accelerometers`

Roque, A. A., Silva, T. A. N., Calado, J. M. F., Dias, J. C. Q., João, R., & Simões, T. (2009). An approach to fault diagnosis of rolling bearings.

Stork, C. L., & Kowalski, B. R. (1999, 3). Distinguishing between process upsets and sensor malfunctions using sensor redundancy. *Chemometrics and Intelligent Laboratory Systems*, *46*, 117-131. doi: 10.1016/S0169-7439(98)00180-4